UNIVERSITY OF AMSTERDAM

UvA-DARE (Digital Academic Repository)

Angle-resolved cathodoluminescence nanoscopy

Coenen, T.

Publication date
2014

Link to publication

Citation for published version (APA):
Coenen, T. (2014). *Angle-resolved cathodoluminescence nanoscopy*. [Thesis, externally prepared, Universiteit van Amsterdam].

General rights
It is not permitted to download or to forward/distribute the text or part of it without the consent of the author(s) and/or copyright holder(s), other than for strictly personal, individual use, unless the work is under an open content license (like Creative Commons).

Disclaimer/Complaints regulations
If you believe that digital publication of certain material infringes any of your rights or (privacy) interests, please let the Library know, stating your reasons. In case of a legitimate complaint, the Library will make the material inaccessible and/or remove it from the website. Please Ask the Library: https://uba.uva.nl/en/contact, or a letter to: Library of the University of Amsterdam, Secretariat, P.O. Box 19185, 1000 GD Amsterdam, The Netherlands. You will be contacted as soon as possible.

UvA-DARE is a service provided by the library of the University of Amsterdam (https://dare.uva.nl)

Download date:04 Nov 2026

4

Directional emission from plasmonic Yagi-Uda antennas probed by angle-resolved cathodoluminescence spectroscopy

Optical nanoantennas mediate optical coupling between single emitters and the far field, making both light emission and reception more effective. Probing the response of a nanoantenna as a function of position requires accurate positioning of a subwavelength sized emitter with known orientation. In this Chapter we use a high-energy electron beam as a broad band point dipole source of visible radiation, to study the emission properties of a Yagi-Uda antenna composed of a linear array of Au nanoparticles. We show angle-resolved emission spectra for different wavelengths and find evidence for directional emission of light that depends strongly on where the antenna is excited. We demonstrate that the experimental results can be explained by a coupled point dipole model which includes the effect of the dielectric substrate.

4.1 Introduction

Plasmonic nanoantennas have gained great interest because of their ability to enhance and redirect light emission from single emitters [29]. Promising applications include spectroscopy [115, 116], single-photon sources, single photon ab-

sorption [117], and light harvesting [118]. A wide variety of different optical antenna geometries have been studied, ranging from single metal nanoparticles [13, 119, 120] to dimers with narrow gaps [38] and more complex multi-element structures [39, 121].

A particularly well-known antenna for radio waves is the Yagi-Uda antenna [33]. Classical Yagi-Uda antennas consist of a single feed element which is actively driven by electrical current and is surrounded by passive resonant scattering elements that couple through dipole-dipole coupling. The collective coherent scattering of the antenna elements can result in a highly directional emitter or receiver [33, 122]. The Yagi-Uda antenna design can be scaled down in size for visible wavelength operation by using metallic nanoparticles, which have a localized surface plasmon resonance, as proposed in Refs. [122–125].

Similar to their radio wave counterparts it has been shown recently that such plasmonic arrays act as efficient nanoscale receiving antennas for light due to dipole-dipole coupling [126, 127]. Confocal microscopy measurements have shown that they have the ability to concentrate an incident light beam at a well-defined wavelength-dependent position on the antenna array [123]. Conversely, it has been shown that metal particle arrays can also be used to direct light into a well-defined wavelength-dependent direction, provided one manages to position a single emitter on a single antenna element [39]. On the basis of these reports, it is anticipated that designed plasmonic and metamaterial clusters can be used to fully control directionality, polarization, and emission rate of single quantum sources.

Optical antenna properties are often probed by using far-field optical microscopy techniques. By their very nature, however, nanoantennas have features much smaller than the wavelength of light making it impossible to spatially resolve their emission properties with free space optics. Several techniques have been developed recently to address this problem. It has been shown that chemically functionalized quantum dots positioned close to an antenna can be effective local probes [39], although controlling the position, quantity, and quality of the quantum dots can be challenging. Nitrogen vacancy centers (NV centers) in nanodiamonds have also been used successfully as local excitation sources of plasmon antennas. Single nanocrystals including NV centers can be positioned at will in nanoantenna geometries using atomic force microscopy tips to position either the NV centers or metal antenna constituents on a substrate [128, 129]. However, it is challenging to obtain full 2D control using this method.

In scanning near field optical microscopy (SNOM) one does have the ability to raster scan the excitation over the antenna [130, 131]. However, for efficient excitation the tip has to be in close proximity to the antenna, thereby perturbing the dielectric environment and thus affecting the experiment. To obtain further insight in the directional behavior of Yagi-Uda antennas, an alternative technique is required, which enables measurements of the angle-resolved response at any desired wavelength and excitation position on a single nanoantenna.

In this Chapter we use a 30 keV electron beam focused to a nanoscale spot

to excite plasmonic Yagi-Uda antennas with a spatial resolution of ~10 nm. We collect the antenna radiation (cathodoluminescence, CL) using a paraboloid mirror integrated in an electron microscope and determine the angle-resolved radiation spectrum, as a function of excitation position. We find evidence for directional photon emission that depends strongly on the excitation position and demonstrate that the experimental results are explained by an analytical point dipole model. The experiment illustrates the potential of angle-resolved CL measurements for the characterization of a wide array of photonic nanostructures.

4.2 Sample fabrication

We fabricated gold nanoparticle antenna arrays consisting of five cylindrical nanoparticles on a crystalline silicon substrate using electron beam lithography and liftoff. We used a 350 nm thick layer of ZEP520A as positive resist for electron beam lithography with a Raith E-line system. After exposure and development, a gold layer was deposited using thermal physical vapor deposition. After lift-off in n-methylpyrollidone (NMP) at 65 °C for 3 h, we obtain gold nanoparticles on silicon with a diameter of 98 nm, a height of 70 nm, and a center-to-center distance of 135 nm. This geometry results in a total length of 638 nm which is roughly equal to one visible wavelength. Figures 4.1(a,b) show a scanning electron micrograph and a schematic representation of the antenna array under investigation.

4.3 Single-particle response

A 30 keV electron beam passes through a hole in a parabolic mirror and irradiates a 10 nm spot on the sample, thereby producing CL emission. The collected CL either can be focused onto a fiber which is connected to a spectrometer (bottom right) or is sent to a 2D CCD array (top right). Defocused arrangement allows us to retrieve angular information (see Chapters 2 and 3 for details).

To find the response of an individual particle, we collect the CL emission as function of excitation position (10 × 10 nm pixel size) for an isolated particle with the same dimensions as the particles in the array. In Fig. 4.1(c) the CL emission spectrum integrated over all excitation positions on the particle is shown. The data were corrected for the wavelength-dependent system response using the transition radiation of a single crystal Au sample [112]. Furthermore the background radiation due to the silicon substrate was subtracted. The spectrum shows one strong peak at 577 nm which we attribute to a dipolar localized surface plasmon resonance along the vertical axis of the cylindrical particle. Note that the resonance is at much shorter wavelength than for similar particles on a silicon substrate under optical excitation [132], which we attribute to the fact that the electron beam excites these particles along their vertical axis.

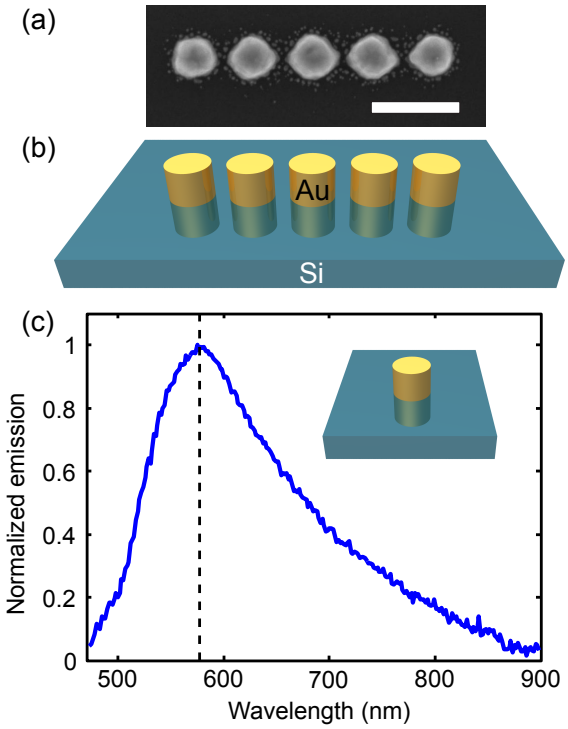


Figure 4.1: (a) Scanning electron micrograph of a plasmonic Yagi-Uda antenna of gold particles (diameter 98 nm, height 70 nm, on Si). Scale bar represents 200 nm. (b) Schematic of the antenna. (c) Normalized CL-emission spectrum as function of wavelength for a single nanoparticle with similar dimensions to the particles in the array. The peak corresponds to 2×10^4 counts/s at 1 nA per 1.7 nm bandwidth.

4.4 Spectral imaging of a Yagi-Uda antenna

To study the spectral response of the antenna, we raster scan the electron beam (1 nA current) over the nanoantenna in 10 nm steps with a dwell time of 0.1 s per pixel and collect an entire visible spectrum at each position. Figure 4.2(a-c) shows the CL intensity as a function of e-beam position for center wavelengths of 500, 600, and 750 nm integrated over a bandwidth of 10 nm. The data were corrected for the silicon background radiation. Evidently the individual particles can clearly be distinguished as excitation points that generate large cathodoluminescence signals in all images. Given the small particle size (~100 nm) compared to the wavelength, the images demonstrate the very high spatial resolution of the CL imaging technique. From the SEM image in Fig. 4.1(a) is it clear that all five particles have approximately the same size, which suggests that they will have similar polarizabilities. However in the images of Fig. 4.2 the outer particles are significantly brighter than the center

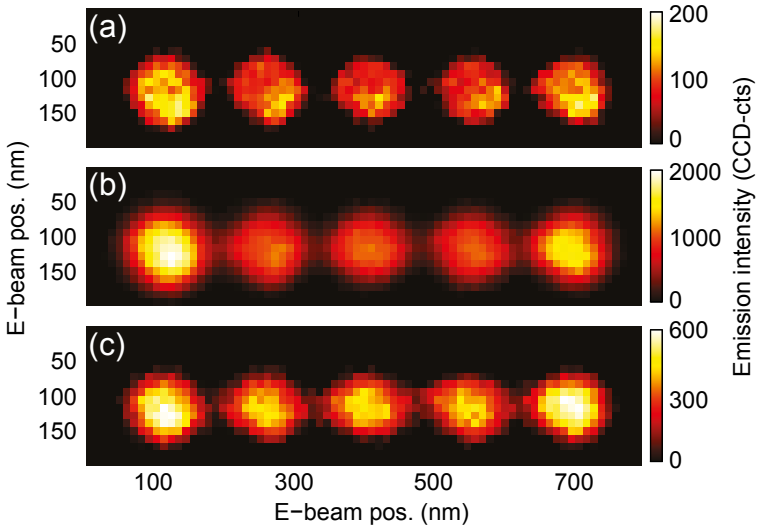


Figure 4.2: Spatially resolved excitation maps of the nanoantenna shown in Figure 4.1a, showing CL intensity as function of e-beam position for (a) 500 nm, (b) 600 nm, and (c) 750 nm detection wavelength integrated over a 10 nm bandwidth. Integration time per pixel is 0.1 s.

particles, with a relative contrast that is highest for λ_0 = 600 nm (emission is ~1.4 times stronger for outer particles). This observation indicates that coupling between the particles is important for the overall emission intensity that is generated upon local excitation.

4.5 Antenna radiation patterns

Next we turn to measuring the radiation pattern of a nanoantenna as a function of wavelength and excitation position, by using the angle-resolved CL collection. To this end, we measure the emission pattern of the antenna for wavelengths from 400 to 750 nm in steps of 50 nm using 40 nm bandpass color filters. To increase the signal-to-noise ratio, we used 2 × 2 hardware binning of the CCD pixels, increased the current to 10 nA, and extended the dwell time to 40 s. We excite each of the five particles in its center and collect a radiation pattern for each of the excitation positions. To eliminate background signal, we subtract a reference measurement from a bare silicon substrate collected using the same color filter and dwell time.

The result of such a measurement for excitation of the outer left particle (see sketch, Fig. 4.3(a)) collected at λ_0 = 500 nm is shown in Fig. 4.3(b). The data are presented in a polar plot where the radius represents θ, the polar angle represents ϕ, and the color scale gives the normalized emission intensity. The measurement

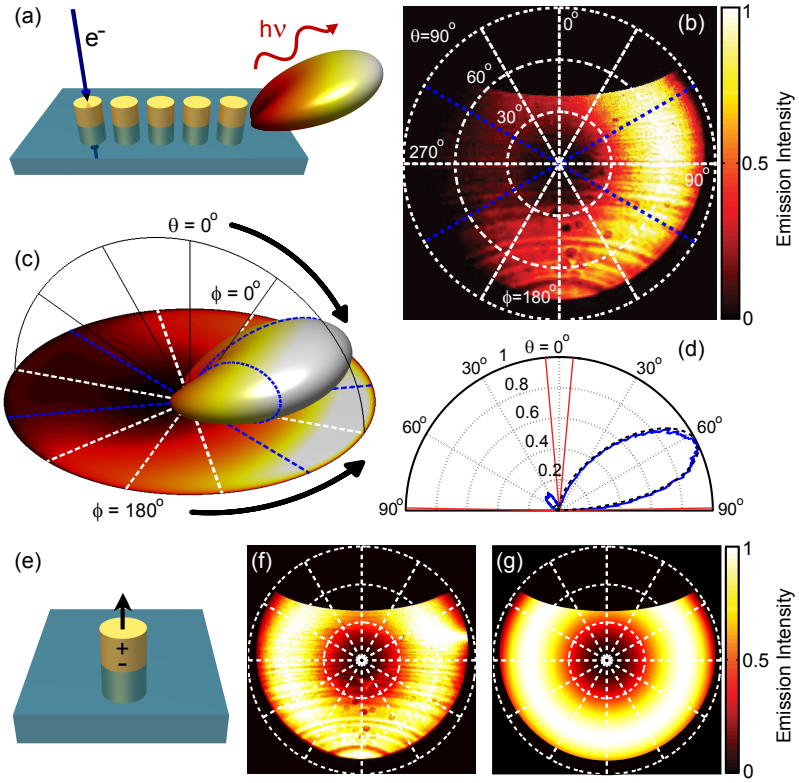


Figure 4.3: (a) Schematic of the excitation geometry. (b) CL emission intensity as a function of angle collected with a 40 nm band-pass filter centered at 500 nm, for excitation of the outer left particle. The blue dashed lines indicate the range of ϕ that is integrated to obtain the crosscut shown in (d). (c) 3D representation of theoretical radiation pattern for this excitation position and wavelength, together with a projection onto a 2D grid. Note that in this projection the spacing of θ is not equidistant like in (b). The blue lines again indicate integration limits for the cross-cut. (d) Cross-cut through the angular data showing CL intensity as a function of θ (blue curve) together with theory (black dashed curve). The red lines indicate the range of θ that cannot be collected by the mirror. (e) Schematic of a single particle which is vertically polarized by the electron beam. (f) CL-emission intensity as a function of angle for a single nanoparticle integrated over all wavelengths (350 – 1000 nm). (g) Calculated emission pattern for a vertically oriented point dipole spaced 35 nm above a silicon substrate, emitting at 577 nm.

reveals that when the leftmost particle is excited, most cathodoluminescence is collected in a single lobe that points toward the right end of the antenna, *i.e.*, to the side away from the excitation point. The dark region that extends from ϕ = 300° to ϕ = 60° for $\theta > 40°$ is due to the fact that we do not collect part of the radiation pattern due to the mirror geometry. Similarly, a small part of the radiation

around $\theta = 0°$ is not collected due to the hole in the mirror that allows the electron beam to pass from the SEM pole piece to sample. To more clearly visualize the directionality of emission that is evident from the polar plot in Fig. 4.3(b), we extract a cross-cut of the data (blue curve) by integrating over ϕ from 60° to 120° and from 240° to 300° yielding CL intensity as function of θ only (Fig. 4.3(d)). This integration omits that part of the hemisphere where we do not collect emission due to the mirror geometry and the part where the aberrations in the mirror are largest (ϕ between 120° and 240°). The cross cut reveals a prominent lobe at θ = 60°, with a width of ~20° that is ~5 times stronger in intensity than the small lobe that extends to the left. For reference we show that the measured radiation pattern of a single nanoparticle is isotropic in ϕ (Fig. 4.3(f)) directly implying that the directionality is due to coupling between particles. Furthermore, the single particle data show that each single particle in the array is equivalent to a vertically oriented dipole above a silicon substrate when excited with the electron beam (see theory in Fig. 4.3(g)) [103].

Figure 4.4 extends the angle-resolved data set shown in Fig. 4.3 to different wavelengths and excitation positions. The top row in Fig. 4.4 shows the radiation patterns for λ_0 = 500, 600, and 750 nm for excitation of the outer left, center, and outer right nanoparticle. The radiation pattern clearly depends strongly both on wavelength and on the position of the electron beam. As expected the emission pattern is roughly mirror symmetric for all wavelengths when the center particle is excited. For excitation of the outer particles, however, the emission is highly directional. Interestingly, the sign of the directionality reverses for increasing wavelength. For 500 and 600 nm the radiation is emitted along the particle array away from the excited particle while for 750 nm it is emitted in the opposite direction (on the side of the excited particle). To our knowledge this data set represents the first measurements in which the directionality of a multielement nanoantenna can be probed and changed at will by moving the excitation spot.

We now turn to the interpretation of our observation that the emission from an Au particle array that is excited at one of its ends is directional. Qualitatively, this switching behavior is well-known for Yagi-Uda arrays [39, 123, 124] and can be explained by the fact that the Yagi-Uda antenna is a traveling wave antenna with a radiation pattern that is the coherent sum of the radiation from each induced dipole in the chain [33, 122]. On one side of the cut-off frequency, the induced phase profile is well matched to forward propagating free photons, leading to beaming away from the excitation point. On the other side of cut-off, interference is destructive in the forward direction, leading to beaming in the backward direction. To interpret the directionality in more detail, we setup a quantitative model. Since the electron beam is azimuthally symmetric, it excites a vertical dipole with the same azimuthal symmetry (also called a $m = 0$ dipole in literature where m in that case is the azimuthal quantum number) in the directly excited nanoparticle on which the electron beam is located [69, 111]. This dipole induces dipole moments in the other particles, and the collective interference of light radiated by all five coherently coupled dipole moments gives rise to the collected radiation pattern.

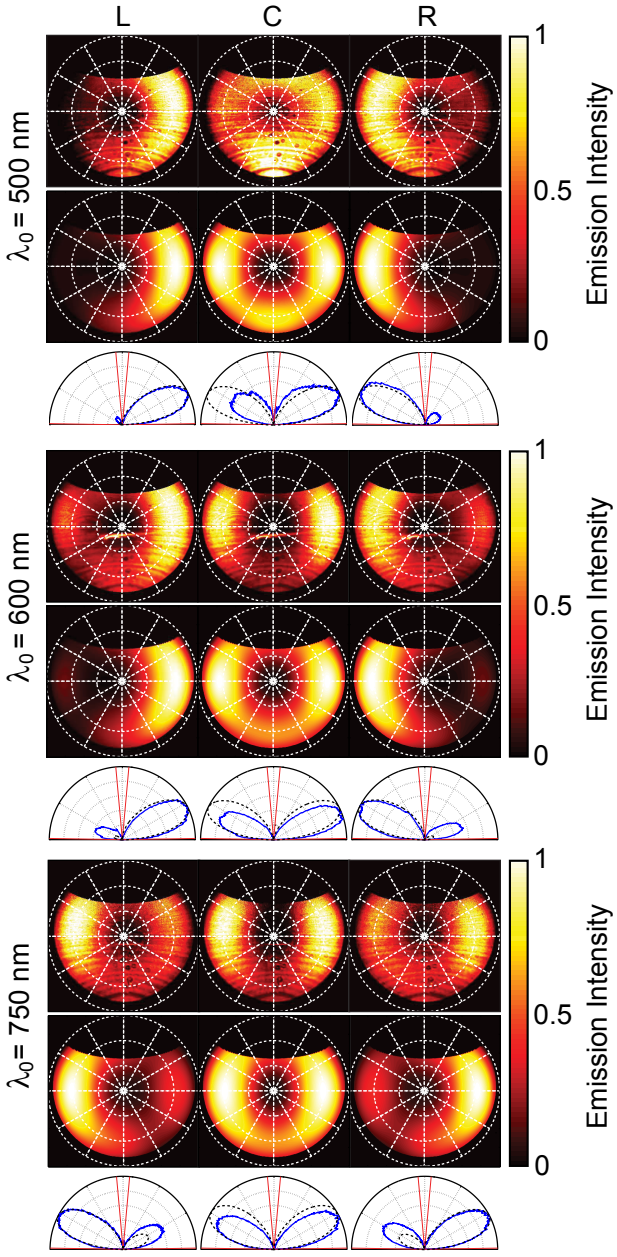


Figure 4.4: Measured angle-resolved emission patterns (top rows), calculated emission patterns (middle rows), and cross-cuts through both (bottom rows) for excitation of the outer left (L), center (C), and outer right (R) particle shown for λ_0 = 500, 600, and 750 nm, respectively.

We note that the refractive index of the silicon substrate is high, so a major portion of the light is scattered into the substrate (~90%) where it cannot be detected. On the other hand the substrate also significantly enhances the LDOS at the position of the dipole, increasing the excitation probability. Hence a significant CL signal is still expected.

4.6 Coupled electrical dipole model

To take into account the coherent coupling, far-field interference, and the influence of the substrate, we setup an analytical point dipole model [123]. In this model, each particle is described as a point dipole that has a dipole moment $\mathbf{p} = \alpha\mathbf{E}$ in response to a driving field $\mathbf{E}$, where the polarizability α contains the plasmon resonance. In a complex array of N particles, the dipole moment induced in particle m is due to the field that is directly induced by the driving E_{in} and the field that is radiated by each other dipole in the array. This realization leads to the following set of equations

$$p_m = \alpha[E_{in} + \sum_{\substack{n=1 \\ n\neq m}}^{N} G(r_m, r_n)\, p_n] \tag{4.1}$$

that can be self-consistently solved to find the induced dipole moment p_m in each particle. In this equation, the Green dyadic $G(r, r')$ quantifies the field at position r due to a dipole located at position r'. Provided one uses the electrodynamic expression for the field of a dipole for $G(r, r')$, and correctly implements radiation damping in the polarizability $\boldsymbol{\alpha}$, this formalism describes scattering to all scattering orders and with correct handling of retardation, interference, and energy balance. In this work, particles are placed at the interface between vacuum and a high index substrate, which strongly influences the radiation. We have successfully implemented this asymmetric environment in a point scattering model, by replacing the Green dyadic of free space

$$G(r, r') = (k^2 + \nabla\nabla)\frac{e^{ik|r-r'|}}{|r-r'|} \tag{4.2}$$

that is ordinarily used [133, 134] in Eq. 4.1 with the Green function for a dielectric interface. We implemented the Green function for a dielectric interface as listed in Ref. [103] (chapter 10) but transformed to cylindrical coordinates, to be optimally equipped to deal with poles that are encountered when performing the required integral over parallel wave vector via contour integration [135]. Once the induced dipole moments are found with aid of $G(r, r')$, we construct the far-field radiation pattern by coherent addition of the far field of each dipole, making use of the asymptotic far-field approximations to $G(r, r')$, discussed in Ref. [103] section 10.6. For the above-mentioned procedure to result in a self-consistent energy-conserving theory, the polarizability also needs to be amended. It is well-known

that if one starts with the electrostatic polarizability of, for instance a plasmon nanosphere in vacuum $\alpha_0 = 3V(\varepsilon - 1)/(\varepsilon + 2)$, one needs to add a dynamic correction (radiation damping) to the polarizability to properly take into account that scatterers lose energy by radiation into the far field [136]. This radiation correction takes the form

$$\frac{1}{\alpha} = \frac{1}{\alpha_0} - \frac{2\imath k^3}{3} \tag{4.3}$$

for particles in a homogeneous environment. The damping term $2\imath k^3/3$ is in fact derived from the local density of optical states, *i.e.*, from $\mathrm{Im}\{G(r,r')\}$, that quantifies how much energy a dipole moment of given strength at position r radiates. By generalizing the radiation damping correction to

$$\frac{1}{\alpha} = \frac{1}{\alpha_0} - \imath\,\mathrm{Im}\{G(r,r')\} \tag{4.4}$$

we obtain a self-consistent theory that satisfies the optical theorem also in the presence of an interface. The following facts should be noted. First, the radiation damping clearly depends on position relative to the interface in proportion to the LDOS defined by the interface. This fact was first realized in an experiment by Buchler *et al.* [137], who measured variations in line width in scattering spectra of a single plasmon sphere as a function of its distance to a mirror. Second, in the above equations, α, α_0 as well as $\mathrm{Im}\{G(r,r')\}$ should all be interpreted as tensors. This tensorial nature is well appreciated for the static polarizability α_0 of anisotropic plasmon particles such as oblate or prolate metal nanoparticles. Interestingly, the orientation dependence of the LDOS that is enclosed in the tensor $\mathrm{Im}\{G(r,r')\}$ implies that even spherical particles with an isotropic geometry specified in α_0 will have an anisotropic electrodynamic response α when brought in proximity to an interface [138]. To model the experiments presented in this work, we use a Lorentzian damped resonance line shape for the static polarizability

$$\alpha_0 = \frac{\omega_0^2}{\omega_0^2 - \omega^2 - \imath\omega\gamma} 4\pi a_0^3 \tag{4.5}$$

Here a_0 is the particle radius, ω_0 the resonance frequency of a single particle, and γ is the intrinsic time constant for material damping. We take the resonance frequency to correspond to the resonance measured by spectrally resolved CL of a single nanoparticle (577 nm, see Fig. 4.1(c)), and set the Ohmic damping rate, γ, to be 8.3×10^{13} s^{-1}, appropriate for gold [139]. For the crystalline silicon substrate tabulated optical constants were used [139]. For E_{in} we use a vertically oriented dipole positioned in the center of one of the nanoparticles (35 nm above the substrate), to mimic the e-beam excitation.

4.7 Comparison between experiment and theory

We use the coupled dipole model to calculate the far-field emission pattern for each wavelength and excitation position. Figure 4.3(c) shows the calculated far field emission for excitation of the leftmost particle, at a wavelength of 500 nm. As in the data, the calculated emission pattern is strongly peaked in the direction away from the excitation point. We extract a cross section through angular integration over the same range as discussed before, which allows us to directly compare experiment and theory. The strong directionality observed in the data is well described by the point dipole model.

Figure 4.4 shows comparisons between theory and experiment for the three wavelengths studied and excitation positions. Overall, the agreement between theory and experiment is excellent for all wavelengths, as evidenced in both polar plots and the cross sections (Fig. 4.4, bottom row). Theory predicts a directional radiation pattern for excitation at the array ends, which for λ_0 = 500 and 600 nm occurs away from the excitation point, and swaps direction for λ_0 = 700 nm, exactly as in the experiment. Additionally, at λ_0 = 500 nm and for excitation of the center particle, the appearance of an extra lobe at $\phi = 180°$ is predicted by the theory which also clearly is present in the data. Moreover, the coupled dipole model correctly predicts that in the angular range presented in Figs. 4.3 and 4.4, most of the radiation is emitted around $\theta = 60°$ (for all three wavelengths in both forward and backward radiating cases). We note that, in contrast to the left/right asymmetry in the radiation pattern, the radiation angle of 60° relative to the surface normal is not dictated by coupling between particles. Indeed, also in the case of a single point dipole emitter 35 nm above a silicon substrate, theory dictates that most of the radiation is emitted around $\theta = 60°$ (see Fig. 4.3(g)) [103]. It is clear from Figure 4.4 (bottom row) that not only the position but also the width of the main emission lobes agrees very well with the theory for both θ and ϕ. Slight discrepancies between theory and data are evident from inspection of the polar maps in Figure 4.4; for excitation of the center particle the measured radiation patterns are not completely symmetric. Furthermore the theory predicts that the radiation should be slightly more unidirectional. Apart from these minor discrepancies between theory and data, which we attribute to fabrication imperfections, the theory reproduces all major features of the experiment. To quantify this agreement further, we calculate the ratio between forward (away from excitation point along the particle array) and backward (toward excitation point) scattered light for both theory and experiment and find that all the experimentally obtained ratios are within a factor 1.3 from the theoretical prediction. The largest experimentally observed ratio (5.3:1) was obtained for excitation of the outer left particle at λ_0 = 500 nm, whereas the smallest ratio (1:1.9) was found for excitation of the outer left particle at λ_0 = 750 nm. The theoretically calculated ratios are 6.7:1 and 1:2.3, respectively. Finally we note that the point dipole model can also be compared to the spatial distributions in Fig. 4.2. By integrating the emission over the angular range collected by the mirror, we obtain the total collected intensity for a particular wavelength and as a

function of the point of excitation. For 600 nm we find that according to theory the contrast in emitted intensity between the outer and center particles should be 1.5. This contrast is very similar to the brightness contrast between the outer and center particles observed in the spatial map of CL intensity in Fig. 4.2. We hence conclude that the CL imaging technique allows one to reliably determine the antenna directionality as well as the radiation strength of the individual dipole elements.

4.8 Conclusions

In conclusion we have used angle-resolved cathodoluminescence spectroscopy to probe both the spectral response and the angular emission of a linear particle array Yagi-Uda antenna upon localized excitation. The electron beam excitation allows one to locally drive the antenna with extremely high spatial resolution (~10 nm) and to probe the response for the entire visible range of the electromagnetic spectrum. The measurements show directional emission which strongly depends on which of the particles is excited and on the free space wavelength. The directionality is a consequence of coherent near-field and far-field interactions between different plasmon resonators in the array. The experimental results can be described accurately by using an analytical coupled dipole model which includes the effect of the silicon substrate. Our work establishes angle-resolved CL spectroscopy as a powerful technique to spatially and spectrally resolve the radiation strength and the directivity of single and composite emitter structures without any ensemble averaging; a unique advantage compared to other techniques.